Influence of surface morphology on the adhesion strength of epoxy–aluminum interfaces

SULIN ZHANG *, RAHUL PANAT and K. JIMMY HSIA [†]

Department of Theoretical and Applied Mechanics University of Illinois, Urbana, IL 61801-2983, USA

Abstract—Adhesively bonded aluminum joints have been increasingly used in the automotive industry because of their structural and functional advantages. Interfacial debonding in these joints has become a major concern limiting their performance. The present work is focused on experimental investigation of the influence of surface morphology on the interfacial fracture behavior of the epoxy–aluminum interface. The specimens used in this experimental study were made of an epoxy–aluminum bimaterial strip in the form of a layered double cantilever beam (LDCB). The LDCB specimens were debonded by peeling off the epoxy layer from the aluminum substrate using a steel wedge. Interfacial fracture energy was extracted from the debonding length using a solution for the specimen geometry based on a model of a beam on an elastic foundation. This model was validated by direct finite element analysis. The experimental results establish a direct correlation between the surface roughness of aluminum substrate and the fracture resistance of the epoxy–aluminum interface. The results emphasize the importance of choosing surface features at an appropriate length scale in studying their effects on interfacial fracture resistance.

Keywords: Adhesive bonding; surface morphology; interfacial fracture resistance; double cantilever beam (DCB); wedge peel test.

1. INTRODUCTION

Adhesively bonded aluminum joints are increasingly becoming popular in aerospace and automotive applications because of their low weight-to-strength ratio and improved manufacturability compared to those made by riveting or welding techniques. Prior to bonding, the aluminum surface is pretreated with certain processes to produce microscale surface morphology. This morphology plays a crucial role in

---

*Current address: Department of Mechanical Engineering, Northwestern University, Evanston, IL 60208, USA.

[†]To whom correspondence should be addressed. Fax: (217) 244-5707. E-mail: kjhsia@uiuc.edu

the fracture behavior of the adhesive bonds [1]. Experiments establishing a relationship between the strength of aluminum−adhesive joints and the aluminum surface morphology are thus highly desirable to guide surface pretreatment processes. Such experiments also provide a fundamental understanding of the interface adhesion and the interface debonding mechanisms.

Extensive experimental [2−22] and modeling [22−25] research has been conducted to study the fracture behavior of various interface systems. These studies have demonstrated the importance of interfacial microstructures in the fracture processes. Turner and co-workers [2, 3] evaluated the adhesion strength of different sandwich systems using double cleavage drilled compression (DCDC) specimens. They observed that for a thermoset polymer−glass interface, the crack propagated by finger-like interface delamination at the crack front. For a sapphire−metal interface, they observed microcavity initiation, growth and coalescence in the metal during crack propagation. Such a process has recently been modeled by Pardoen and Hutchinson [26] and Zhang and co-workers [27, 28]. Cazzato and Faber [4] observed that during fracture of a glass−alumina interface, the crack path was not restricted to the interface, resulting in fracture resistance being almost independent of the alumina surface roughness. Note that in all the above investigations [2−4], the fracture energies measured for the interfaces were on the order of tens of J/m^2. Thouless [5, 6] studied the importance of the local phase angle in determining the interfacial fracture resistance. He concluded that the degree of the adherend surface roughness as well as the mode-mixity determined the interfacial fracture resistance, while the thickness of the adhesive had negligible effect on the interfacial fracture resistance.

Interfacial fracture behavior of the epoxy−metal interfaces has been studied by several researchers [9−15, 18, 19]. Price and Sargent [9] found that increasing the thickness of epoxy on an aluminum substrate enhanced the peel strength of the specimens. Chai [10, 11] investigated the effect of epoxy thickness on the adhesive joints using double cantilever beam (DCB) specimens with aluminum and a laminated composite as the adherends. He found that the fracture energy variation with the adhesive thickness depended on the adhesive properties: specimens having brittle adhesives showed little variation while those with thermoplastic adhesives showed significant variation. Chai [12] also demonstrated that mode-mixity in these adhesive joints played an important role in crack path determination during interfacial fracture. Brewis and Critchlow [13] established a direct relationship between electrochemical pretreatment of aluminum surfaces and the peel force of delamination of T-peel joints for various adhesives. The surface morphologies due to the surface pretreatments, however, remained to be characterized in their study. Kalnins *et al.* [14] investigated the effects of surface roughness on the peel strength of a steel−epoxy−steel sandwich specimen. They characterized the steel surface roughness using idealized geometries to approximate the actual surface features as observed under a scanning electron microscope (SEM). The peel strength of the specimens was found to increase with the surface roughness parameter based on

these idealized geometries. The above authors [9, 13, 14] did not use interfacial fracture parameters in their analysis, making it difficult to generalize the results. Mannelqvist and Groth [18] used fractal analysis to characterize the roughness of the steel surface in studying the adhesion strength of epoxy–steel interfaces. The tensile strength was generally found to increase with the fractal dimension. Zhang and Spinks [15] used a lap shear test to measure the effect of surface roughness on the fracture energy of an epoxy–aluminum interface, where the aluminum surfaces were pretreated using the Forest Products Laboratory etching procedure (FPL). The fracture energy was found to be between 29 and 263 J/m^2 and was nearly linearly proportional to the fraction of the aluminum area etched by the FPL procedure. They attributed the increase of interfacial fracture resistance exclusively to the increase of the surface area of the aluminum due to etching. Sancaktar and Gomatam [19] measured the strength of a single lap joint made of steel, Epon 815, and Epon 830. The steel surface was etched to produce microroughness. They found that the strength of the joint was generally enhanced as the surface roughness increased. In spite of all these studies, the underlying fracture mechanisms related to the surface roughness that cause the delamination of layered structures remain to be investigated.

In the present work, a systematic study was undertaken to investigate the effects of various aluminum surface morphologies on the fracture resistance of the epoxy–aluminum interface. The specimen geometry was chosen to be a bi-layer double cantilever beam (LDCB), with epoxy and aluminum forming the two layers. The LDCB specimen geometry had several advantages over DCB [29], four-point flexural [30], and DCDC [2] specimen geometries. The interfacial fracture resistance calculations were simple for the LDCB geometry. A stable crack propagation could be readily achieved in the LDCB specimens. The debond front could also be monitored optically for this geometry. Finally, a sharp interfacial precrack could be generated in LDCB geometry by simply inserting a wedge between the epoxy and the aluminum. In DCDC specimen geometry, a sharp precrack is generated by fatigue loading [2, 3, 31, 32]. The epoxy–aluminum interface, being relatively insensitive to fatigue loading, is not suitable for DCDC geometry. Present study focuses on identifying the possible interfacial fracture mechanisms affecting the adhesion strength.

2. EXPERIMENTAL

2.1. Material system

The bi-layer material system chosen for this study consisted of an Al alloy (6061) and an epoxy adhesive (DP270, 3M, St. Paul, MN, USA). The composition of the alloy is given elsewhere [33]. The properties of the epoxy can be obtained from the 3M website (http://www.3m.com). The Young's modulus of the epoxy was determined by a compression test on a cylindrical bar, 18.8 mm in diameter and
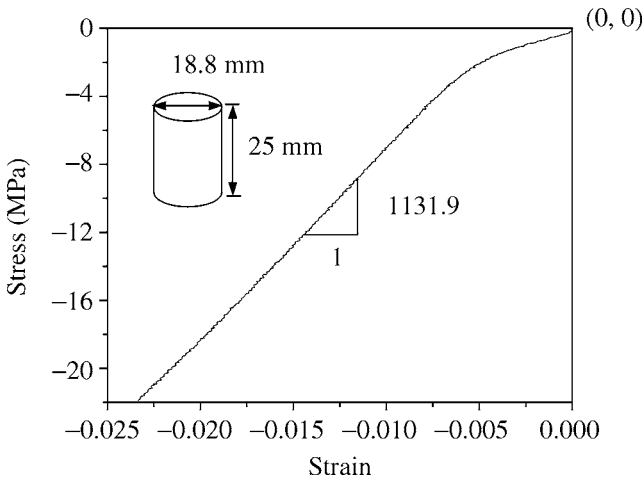
Figure 1. Stress–strain curve for the fully-cured epoxy (DP270). The inset shows the dimensions of cylindrical bar of the epoxy that was loaded along the circular faces to obtain the curve.

25 mm in length, on a universal testing machine (UTM) (Instron, Canton, MA, USA). Before the compression test, the epoxy was heated to 160°C with a hold time of about 2 hours, and then was furnace-cooled and left at room temperature for two days. This process fully cured the epoxy. The fully-cured epoxy was off-white, facilitating visualization of the crack front in the fracture experiment. The stress–strain curve measured by the UTM is shown in Fig. 1. The Young modulus of the epoxy is taken as the slope of the linear portion of the curve since this value of 1131.9 MPa is only a fraction of the stiffness of the loading mechanism of the UTM. The Poisson ratio for the epoxy is about 0.4 [34].

2.2. Specimen preparation

Different surface morphologies of the aluminum alloy were produced and categorized into two groups based on the surface preparation process used. The first and second groups were made from aluminum plates of thickness 4 mm and 2 mm, respectively. One side of each of the plates was polished down to 1 μm diamond paste. As a baseline surface condition, the surface morphology of the polished aluminum surface and its line scan are shown in Fig. 2. The amplitude of surface roughness is on the order of 75 nm. These plates were sliced into rectangular pieces, 55 mm long and 5 mm wide. The polished surfaces of the first group were repolished using different grits SiC grinding papers (No. 60, 180, 320 and 600, Buehler, Lake Bluff, IL, USA). The polishing direction was perpendicular to the crack propagation direction of the specimens. For comparison, aluminum specimens without any repolishing were also included in the first group. A representative surface polished with 600-grit paper is shown in Fig. 3. For the second group, the polished aluminum surface was oxidized using a coaxial rotating, axially translating electrochemical reactor (CRATER) developed by Gao *et al.* [35, 36]. This oxidation process was used to
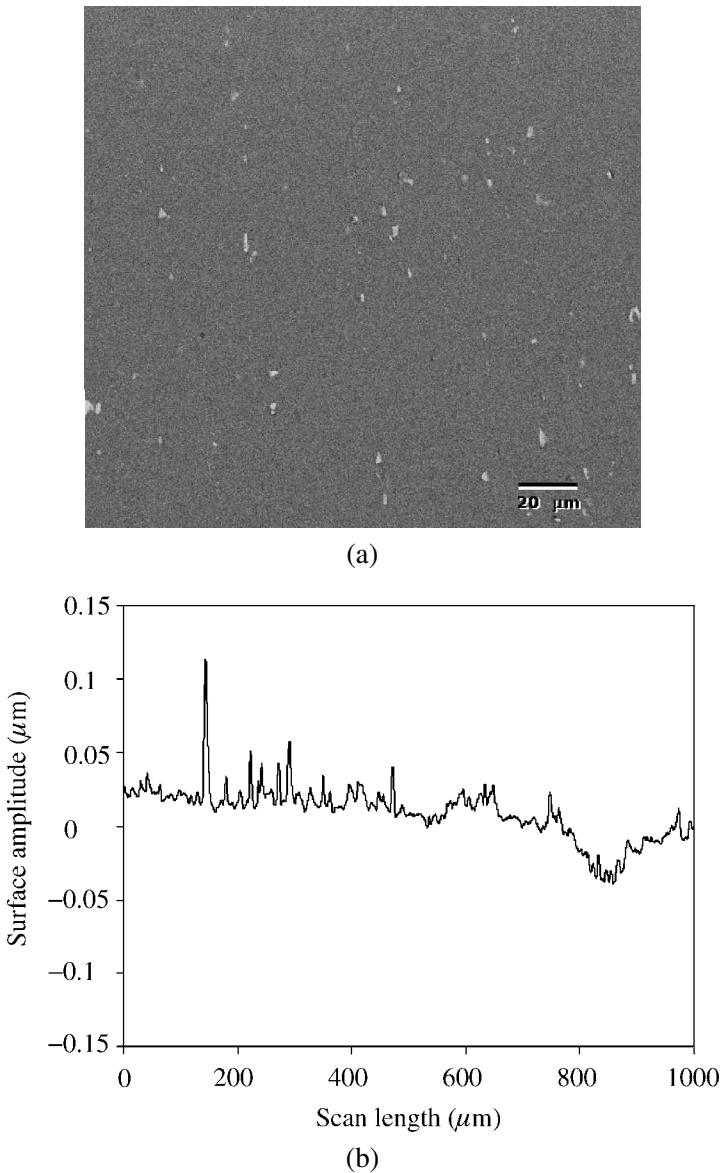
(a)

(b)

Figure 2. Aluminum surface polished by 1 μm diamond paste. (a) Scanning electron micrograph; (b) line scan recorded by a profilometer.

produce three types of surface morphologies, each with uniformly distributed pores of approximately 15, 25, and 40 nm in size, corresponding to applied voltages of 2.8, 5.8 and 9.6 V, respectively. A representative surface morphology from the second group is shown in Fig. 4. Other than the difference in surface treatment methods, the only difference between the specimens in the first and the second groups is their thicknesses. In addition, a one-side finely-polished sapphire sample (Coating &
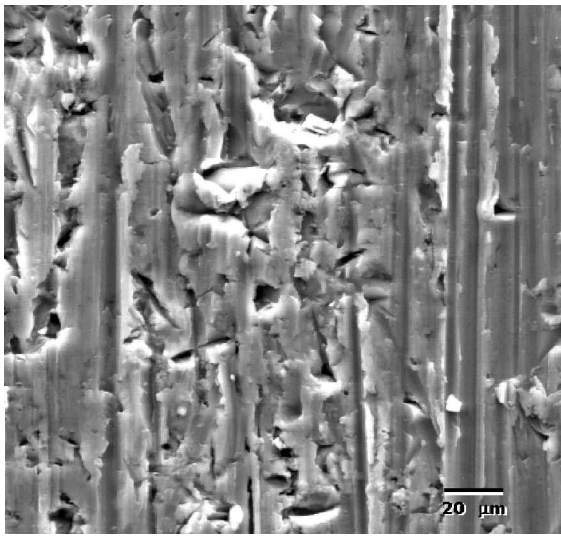
(a)
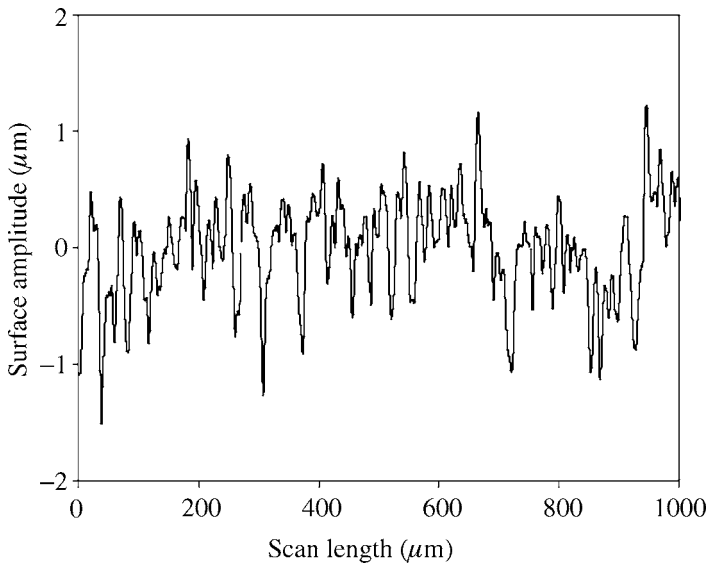
(b)

Figure 3. Aluminum surface polished by 600-grit SiC paper. (a) Scanning electron micrograph; (b) line scan recorded by a profilometer.

Crystal Technology, Kittanning, PA, USA) with dimensions identical to the aluminum specimens in the second group was used in this study to provide a baseline value of fracture resistance.

For clarity, the specimens mentioned above were categorized in terms of the surface treatment used. An identification number was assigned to each type of
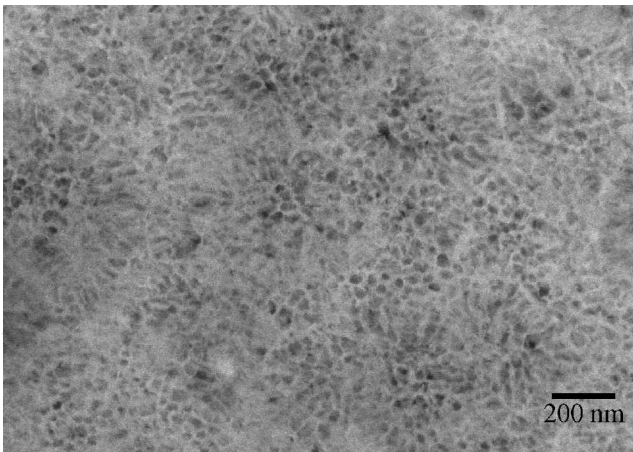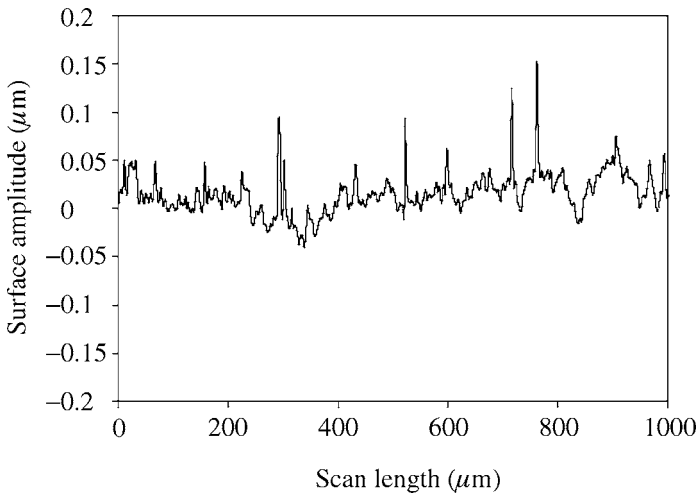
Figure 4. Aluminum surface oxidized by CRATER (applied potential 9.6 V). (a) Scanning electron micrograph; (b) line scan recorded by a profilometer.

specimen, as listed in Table 1. Sample identifications starting with 'G' and 'D' fall in the first group, while those starting with 'O' fall in the second. Table 1 gives the surface treatment method applied and the roughness index for each type of the samples. The roughness index, R, of the surface is defined as [14, 19, 37]:

$$R = \frac{\Delta A}{A_0}, \tag{1}$$

where the area increment, $\Delta A = A - A_0$, with A being the real surface area of the aluminum surface and A_0 being the corresponding projected surface area.

Table 1.
Surface treatment and roughness index

Specimen ID	Surface treatment	Roughness index (R)
SA-1	Sapphire surface	2.82E−07
O2-2	CRATER (2.8 V)	4.69E−05
O5-3	CRATER (5.8 V)	3.08E−05
O9-4	CRATER (9.6 V)	6.11E−05
DP-5	1 μm finish	3.89E−06
G600	600 grit finish	4.79E−03
G320	320 grit finish	2.90E−02
G180	180 grit finish	2.87E−02
G60	60 grit finish	5.84E−02

The aluminum slices were coated with a 2 mm thick epoxy layer to form LDCB specimens. The epoxy in these specimens was fully cured by a process identical to that used for the epoxy cylindrical bar. Extra epoxy on the specimens was carefully polished off. Furthermore, the side surfaces of the specimens were polished by 600-grit SiC paper to enhance crack-tip visualization.

2.3. Surface characterization

Morphology of the pretreated aluminum surfaces was characterized by line scans in the crack propagation direction using a profilometer (Dektak, Sloan Technology, Santa Barbara, CA, USA) at the Frederick Seitz Materials Research Laboratory (FSMRL), University of Illinois at Urbana-Champaign (UIUC). Several scans, each with a full scale of 1000 μm were taken for each type of the aluminum surface. This scan scale is thought to be long enough to capture the characteristic surface fluctuations of interest. The actual distance along the scan line is calculated by numerical integration of the data points. The roughness index is then approximated by the ratio, $\Delta l / l_0$, where Δl is the length increment of the actual surface, while l_0 is the corresponding projected scan line length. The roughness index value for each of the surfaces listed in Table 1 represents the statistical average of that obtained from at least four line scans. Atomic force microscopy (AFM) was also used to characterize the surface of the specimen O9-4 at different resolutions, as discussed in Section 6.

2.4. Test apparatus and procedure

Figure 5 shows a picture of the test apparatus (Fig. 5a) along with a schematic (Fig. 5b). The apparatus consists of two micrometers, a stationary base, and three translation stages, denoted by M-1, M-2, SB, TS-1, TS-2 and TS-3, respectively. M-1 and M-2, that control TS-1 and TS-2, are not shown in Fig. 5b. The translation
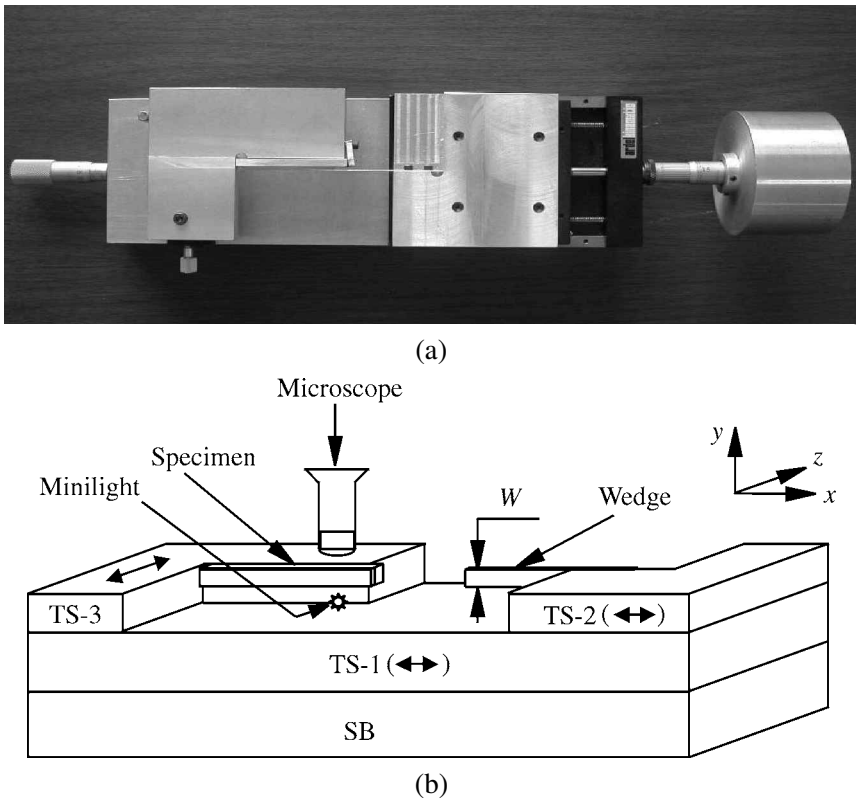
(a)

(b)

Figure 5. Test apparatus. (a) Image (top view); (b) schematic.

stage TS-1 is mounted onto SB, and is movable in the x-direction ($0-40$ mm range). It serves as a master stage on which TS-2 and TS-3 are mounted. The translation stage TS-2 is also movable in the x-direction ($0-25$ mm range). The positions of TS-1 and TS-2 can be determined from the micrometers (M-1 and M-2) with an accuracy of 0.01 mm.

A wedge made of high speed tool steel (T-series) is attached to a fixture, which is mounted onto TS-2. The wedge is 15 mm long, 0.8 mm thick and has a width W approximately equal to that of the specimens. Specimens are held by a fixture that is mounted on TS-3 with the interface of interest being in the $x-y$ plane. The translation stage TS-3 is movable in the z direction with a 6 mm translation capacity. By adjusting TS-3, the epoxy–aluminum interface is aligned with the wedge.

A Nikon optical microscope is positioned above the test apparatus to monitor the moving crack tip. Aided by a mini-light placed at the bottom of the specimen, a video camera at the side of the specimen records the crack front through the off-white epoxy thickness.

Before mounting a specimen onto the fixture, it is precracked on one end by a sharp blade. The length of the precrack, a_0, is recorded using the microscope. Then, TS-1 and TS-2 are both adjusted to their extreme positions while placing the crack

tip in the view of the microscope. During testing, by adjusting TS-1, the crack tip remains within the view of the microscope. The crack length, a, defined as the linear distance from the crack tip to the wedge tip, can be determined by

$$a = a_0 + [s - s_0] - [q - q_0], \tag{2}$$

where s_0 and q_0 are, respectively, the initial positions of TS-1 and TS-2, corresponding to a_0, while s and q are, respectively, the current positions of TS-1 and TS-2, corresponding to a.

The interfacial crack propagation was accomplished by pushing the wedge along the epoxy–aluminum interface. The interfacial fracture energy was evaluated by measuring the crack length as described in the following section. The effects of surface morphology on fracture energy were studied by carrying out the experiments on specimens with different surface treatments listed in Section 2.2.

3. ENERGY RELEASE RATE

Interfacial fracture resistance, $\mathcal{G}_c$, can be evaluated by measuring the critical energy release rate at the onset of stable crack growth. For the specimen schematically shown in Fig. 6, the energy release rate, $\mathcal{G}$, can be expressed as a function of the geometry of the specimen and the material constants, as

$$\frac{\mathcal{G}}{E_{ep}h_{ep}} = F\left(\frac{a}{h_{ep}}, \frac{c}{h_{ep}}, \frac{\delta_y}{h_{ep}}, \frac{h_{Al}}{h_{ep}}, \frac{E_{ep}}{E_{Al}}\right), \tag{3}$$

where h_{ep}, h_{Al} and δ_y are the thicknesses of the epoxy, the aluminum substrate and the wedge, respectively, c is the length of the bonded portion of the epoxy, l is the
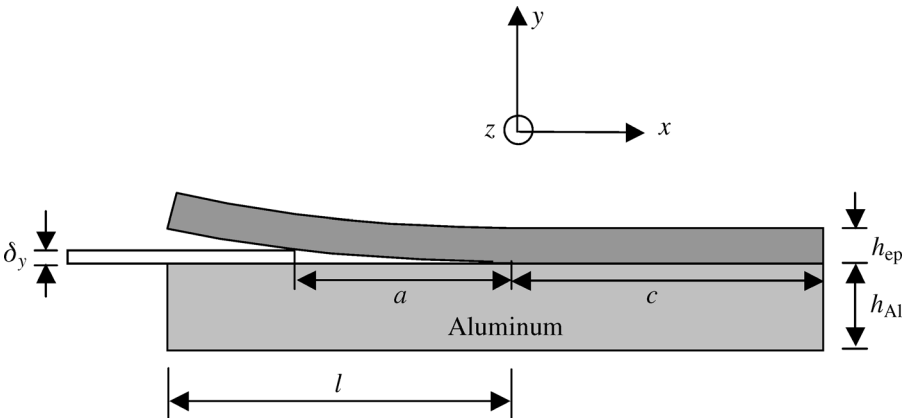

Figure 6. Schematic of the layered double cantilever beam (LDCB) specimen.

total length of debonded portion, while E_{ep} and E_{Al} are the Young's moduli of the epoxy and aluminum, respectively.

The dimensionless function in equation (3) can be approximately evaluated by three different methods, as described below.

3.1. Simple beam theory

Since aluminum substrate ($E_{Al} = 69$ GPa) is much stiffer than epoxy ($E_{ep} = 1.13$ GPa), elastic strain energy stored in the aluminum substrate may be neglected as a first approximation. The debonded portion of the epoxy can be modeled as a cantilever beam. The reaction force, F_y, corresponding to the applied displacement, δ_y, at the contact point between the wedge and the epoxy can be written as

$$F_y = \frac{E_{ep}\delta_y b}{4}\left(\frac{h_{ep}}{a}\right)^3,\tag{4}$$

where b is the width of the epoxy (or aluminum) beam in the z-direction in Fig. 6. By definition, the compliance of the beam is

$$C_0 = \frac{\delta_y}{F_y} = \frac{4a^3}{E_{ep}bh_{ep}^3}.\tag{5}$$

The energy stored in the epoxy beam, Λ, is

$$\Lambda = \frac{1}{2}\frac{\delta_y^2}{C_0} = \frac{E_{ep}b}{8}\left(\frac{h_{ep}}{a}\right)^3\delta_y^2.\tag{6}$$

The energy release rate $\mathcal{G}$ is given by

$$\mathcal{G} = -\frac{1}{b}\frac{\partial\Lambda}{\partial a} = \frac{3}{8}E_{ep}\left(\frac{h_{ep}}{a}\right)^3\frac{\delta_y^2}{a}.\tag{7}$$

3.2. Beam on an elastic foundation

To estimate the energy release rate using the simple beam theory is a good approximation only when the effective crack length, a, is at least five times the thickness of the epoxy beam. Moreover, modeling the unbonded portion of the beam as a clamped end overestimates the stiffness of the structure, leading to an overestimation of the energy release rate. For a more accurate estimate, the energy stored in the bonded portion needs to be taken into account.

Kanninen [38] proposed an approach for determining the energy release rate of such an LDCB specimen. This approach models the specimen as a beam partially free and partially supported by an elastic foundation with stiffness k (see Fig. 7). To establish the relationship between the applied load and the displacement at the loading point, one can invoke the following governing equations for the beam
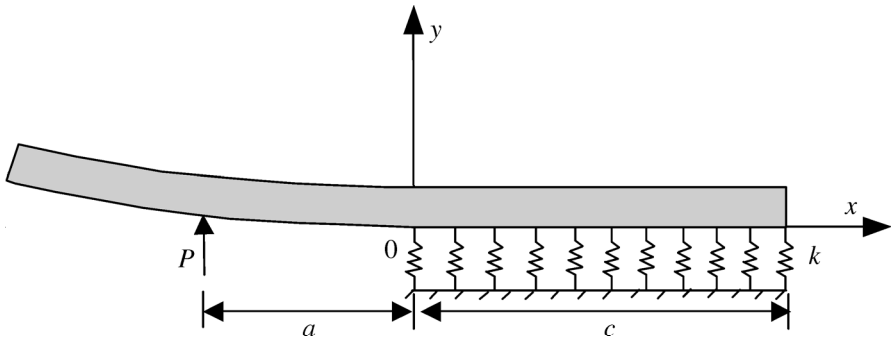
Figure 7. Beam on an elastic foundation.

deflection $w(x)$,

$$\frac{\mathrm{d}^4 w}{\mathrm{d}x^4} + 4\lambda^4 H(x) w = 0, \tag{8}$$

where $H(x)$ is a step function defined as

$$H(x) = \begin{cases} 1, & x > 0 \\ 0, & x \leqslant 0, \end{cases}$$

and

$$\lambda = \left(\frac{k}{4 E_{\text{ep}} I_{\text{ep}}}\right)^{1/4},$$

where I_{ep} is the bending moment of inertia of the epoxy beam.

The appropriate boundary conditions are a shear force P at the loading point (the wedge tip) and a homogeneous boundary condition at $x = c$, as

$$w''(-a) = 0, \tag{9}$$

$$w'''(-a) = P/E_{\text{ep}} I_{\text{ep}}, \tag{10}$$

$$w''(c) = w'''(c) = 0, \tag{11}$$

where c is the portion of the beam supported by the elastic foundation (Fig. 7).

Details of the solution of the above equations are given in Kanninen [38] and Dai et al. [39]. The solution establishes a relationship between the applied load and the displacement at the loading point. The compliance of the structure can be obtained as

$$C_p = \frac{w(-a)}{P} = C_0 \Phi, \tag{12}$$

where

$$\Phi = 1.0 + k_1 \frac{h_{\text{ep}}}{a} + k_2 \frac{h_{\text{ep}}^2}{a^2} + k_3 \frac{h_{\text{ep}}^3}{a^3} \tag{13}$$

and

$$k_1 = \frac{3}{\lambda h_{\text{ep}}} \left(\frac{\sinh \lambda c \cosh \lambda c + \sin \lambda c \cos \lambda c}{\sinh^2 \lambda c - \sin^2 \lambda c} \right), \tag{14}$$

$$k_2 = \frac{3}{\lambda^2 h_{\text{ep}}^2} \left(\frac{\sinh^2 \lambda c + \sin^2 \lambda c}{\sinh^2 \lambda c - \sin^2 \lambda c} \right), \tag{15}$$

$$k_3 = \frac{3}{2\lambda^3 h_{\text{ep}}^3} \left(\frac{\sinh \lambda c \cosh \lambda c - \sin \lambda c \cos \lambda c}{\sinh^2 \lambda c - \sin^2 \lambda c} \right). \tag{16}$$

The foundation stiffness, k, can be estimated by assuming the aluminum substrate as a series of springs. The deflection that defines the transverse displacement of the central line of the epoxy beam is due to the stretching of the elastic foundation, i.e.

$$\sigma(x) = \frac{kw(x)}{b} = \frac{E_{\text{Al}} w(x)}{h_{\text{Al}}}, \tag{17}$$

where $\sigma(x)$ is the load on the aluminum substrate per unit length in x-direction (Figs 6 and 7). From equation (17), one has

$$k = \frac{E_{\text{Al}} b}{h_{\text{Al}}}, \tag{18}$$

and

$$\lambda = \frac{1}{h_{\text{ep}}} \left(\frac{3 E_{\text{Al}} h_{\text{ep}}}{E_{\text{ep}} h_{\text{Al}}} \right)^{1/4}. \tag{19}$$

The strain energy can be written as

$$\Lambda = \frac{1}{2} \frac{\delta_y^2}{C_p}, \tag{20}$$

and the energy release rate is

$$\mathcal{G} = \frac{1}{2b} \frac{\delta_y^2}{C_p^2} \left[\Phi \frac{\partial C_0}{\partial a} + C_0 \frac{\partial \Phi}{\partial a} \right] = \frac{3C_0}{2ab} \frac{\delta_y^2}{C_p^2} \left[1 + \frac{2}{3} k_1 \frac{h_{\text{ep}}}{a} + \frac{1}{3} k_2 \frac{h_{\text{ep}}^2}{a^2} \right]. \tag{21}$$

Note that the energy release rate is independent of the parameter k_3. The energy release rate predicted by this model can always be reduced to that obtained by the simple beam theory by assuming the elastic foundation to be infinitely stiff, i.e. by letting $\lambda \to \infty$, with vanishing k_1, k_2 and k_3.

Our calculation for different values of c shows that the energy release rate is nearly independent of c provided that $c \geqslant 2h_{\text{ep}} = 4$ mm. For simplicity, all calculations are based on the condition of $c \gg h_{\text{ep}}$. For the specimen configurations, our calculations give

$$k_1 = 0.974, \quad k_2 = 0.316, \quad k_3 = 0.051, \tag{22}$$

for the specimens in the first group (polished by SiC grinding paper) and

$$k_1 = 0.819, \quad k_2 = 0.224, \quad k_3 = 0.031, \tag{23}$$

for the specimens in the second group (treated with CRATER electrochemical oxidation).

3.3. Finite-element analysis

A finite-element model was constructed using ANSYS (version 5.7) to analyze the specimens and verify the theoretical models. Plane-strain condition was applied in this analysis. At the tail of the crack, a displacement $\delta_y = 0.8$ mm in the y direction was prescribed at the bottom side of the epoxy beam. The effective crack length was taken in the range of $5-20$ mm. Six-node, triangular elements were used for both the epoxy beam and aluminum substrate. Two approaches were used to calculate the energy release rate, as presented below.

3.3.1. Stress method. The stress method calculates the stress field accurately in the vicinity of the crack-tip by refining the mesh in that region. To ensure accurate estimation of the energy release rate, the element size around the crack tip must be at least 10^{-3} times typical dimension of the specimen (e.g. the thickness h_{ep}). Furthermore, to estimate the stress intensity factors K_I and K_{II} accurately, the stress values for the first 7 to 10 elements from the crack-tip should not be used. In our analysis, stresses in the 10th and subsequent elements ahead of the crack-tip were used to calculate the stress intensity factors. The boundary conditions are such that the displacements of the ends of aluminum substrate are zero. The energy release rate is then calculated using the stress intensity factors [24]. Our result shows that, at a given effective crack length a, the energy release rate is nearly independent of the total debonding length, l.

Mode-mixity is an important parameter for interfacial cracks [24]. According to our numerical analysis, the mode-mixity of LDCB specimen is nearly independent of the thickness of the aluminum substrate, and weakly dependent on the effective crack length. For the effective crack length ranging from 8 to 20 mm, the mode-mixity falls in the range of $-42 \pm 2°$.

3.3.2. Energy method. The energy method estimates the elastic strain energy stored in two similar configurations. These two geometries, denoted by I and II, differ only in the effective crack length, denoted by a_I and a_{II}, respectively $(a_{II} - a_I = \Delta a)$. The boundary conditions are the same as those used in the stress method. Analyzing each configuration with the same mesh density, one can obtain the values of total strain energy of the epoxy–aluminum substrate system. By definition, the energy release rate can be estimated by

$$\mathcal{G} = -\frac{\Lambda_{II} - \Lambda_I}{\Delta a}, \tag{24}$$

where Λ_I and Λ_{II} are the strain energies stored in configurations I and II, respectively. In the calculation, the energy release rate converges quickly as Δa decreases. When Δa is in the range of 1% to 0.5% of a_I, the variation of the energy release rate is negligibly small. In our calculations, Δa is consistently taken to be 0.5% of a_I.

An advantage of this approach is that it does not require ultra-fine mesh at the crack-tip, thus significantly reducing the computational complexity. However, the calculated stress at the crack-tip is not accurate due to the coarse mesh used, and hence cannot be used to estimate the mode-mixity. Our numerical results demonstrate that the values of the energy release rate calculated by the stress and energy methods are within 1.5% of each other, validating both methods.

3.4. Comparison

The energy release rate as a function of the effective crack length obtained from the three approaches is presented in Fig. 8. It shows that, when the effective crack length is greater than 12 mm, all three methods give approximately the same energy release rate data. For an effective crack length less than 9 mm, the simple beam theory predicts higher energy release rate than the other two methods. However, the 'beam on an elastic foundation' model predicts an energy release rate of less than 5% in difference from that obtained by finite-element analysis, provided that the effective crack length is greater than 6 mm.
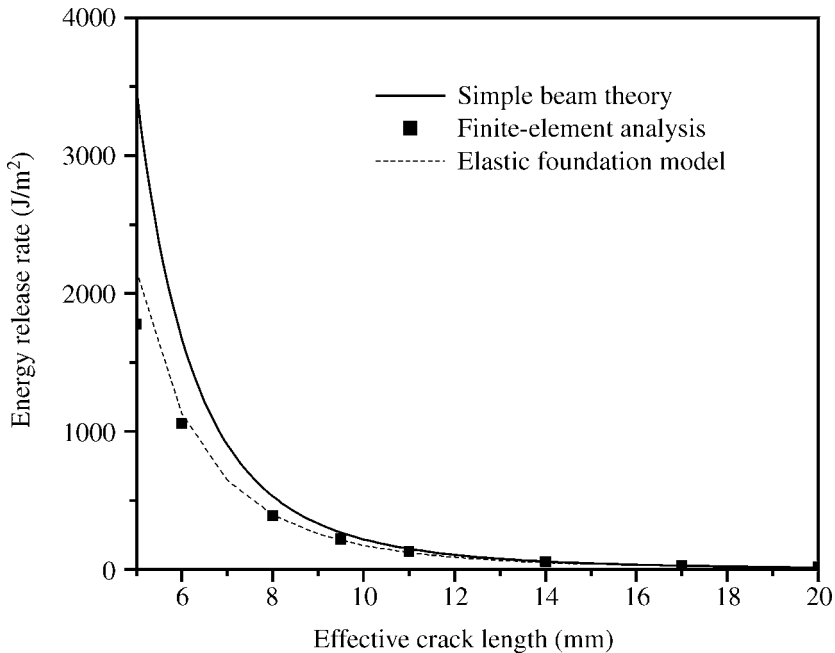

Figure 8. Energy release rate as a function of the effective crack length.

4. EFFECT OF FRICTION AND SHRINKAGE

A major concern with the wedge peel test is the friction between the wedge and the specimen. Such a friction provides an extra driving mechanism for interfacial crack propagation. To validate the energy release rate calculated for the LDCB specimen, one needs to estimate the effect of friction. The frictional force, F_f, can be estimated from the reaction force, F_y, at the wedge end, as

$$F_f = \mu F_y, \tag{25}$$

where μ is the friction coefficient between the wedge and the epoxy. A simple test involving sliding the epoxy on an inclined steel surface gives $\mu \approx 0.3$. The displacement in the horizontal direction, δ_x, due to the friction force can be calculated by

$$\delta_x = \frac{F_f a}{E_{ep} b h_{ep}} + \frac{F_f h_{ep}^2 a}{4 E_{ep} I_{ep}} = \frac{4 F_f a}{E_{ep} b h_{ep}}. \tag{26}$$

The first term on the right-hand side in equation (26) results from the axial deformation, while the second term comes from bending. Substituting equations (4) and (25) into equation (26), one has

$$\delta_x = \mu \left(\frac{h_{ep}}{a} \right)^2 \delta_y. \tag{27}$$

The energy stored in the epoxy beam due to the frictional force is

$$\Lambda_f = \frac{1}{2} F_f \delta_x = \frac{\mu^2 E_{ep} b}{8} \left(\frac{h_{ep}}{a} \right)^5 \delta_y^2. \tag{28}$$

From equation (6) one has

$$\frac{\Lambda_f}{\Lambda} = \mu^2 \left(\frac{h_{ep}}{a} \right)^2. \tag{29}$$

Equation (29) shows that the energy stored in the epoxy beam due to friction is negligibly small compared to bending energy stored in the epoxy beam, even for high friction coefficients.

During the curing process, the epoxy layer is expected to shrink. This shrinkage is constrained to a thin layer of epoxy adjoining the epoxy–aluminum interface. When the crack propagates, this energy will be released in addition to that calculated in Section 3. The cure shrinkage of the epoxy was about 0.08 % (Material Data Sheet for DP270, 3M website). Using the value of the measured epoxy modulus (1131.9 MPa, Fig. 1) and assuming that the thickness of the constrained layer is less than 1 mm, the energy associated with shrinkage is less than 1% of the bending energy stored in the epoxy beam. Thus, frictional effect and epoxy shrinkage are ignored in the calculation of the energy release rate.

5. RESULTS

Due to stress relaxation in the epoxy, the crack length measured in the experiment is dependent on loading rate, i.e. wedge velocity. Experiments using DP-5 specimens show that, for loading rates higher than about 1.2 mm/s, the effective crack length remains almost unchanged. To avoid loading rate dependence, all the experiments were carried out in the present work using a loading rate higher than about 1.5 mm/s. All the tests were run at room temperature (about 21°C) in ambient air.

Optical observations during the tests revealed that initial debonding occurred in the form of small patches ahead of the crack tip upon pushing the wedge, as seen in Fig. 9 for a G60 specimen. These patches coalesce upon pushing the wedge further, and eventually connect to the main crack. New debonded patches would then start to form ahead of the new crack front. The crack, therefore, propagates in a jerky manner, jumping intermittently as it grows. The jerkiness during crack propagation is influenced by the surface morphologies of the aluminum substrate, consistent with the experimental observations by Turner and Evans [3]. In general, rougher surfaces give rise to bigger jumps, whereas smoother surfaces result in smaller jumps for a given wedge speed. It is expected that some plastic flow must be present at the crack front preceding each crack jump. Examinations of fracture surfaces by an optical microscope revealed no epoxy on the smoother aluminum surfaces, while isolated epoxy patches could be seen occasionally on the rougher surfaces.

A representative debonding front highlighted by a black dye penetrant as observed using the video camera is shown in Fig. 10. The crack front exhibits a typical arc-like shape, indicating a plane-stress condition on the side surface of the specimen, and a plane-strain condition near the center. When measuring the crack length
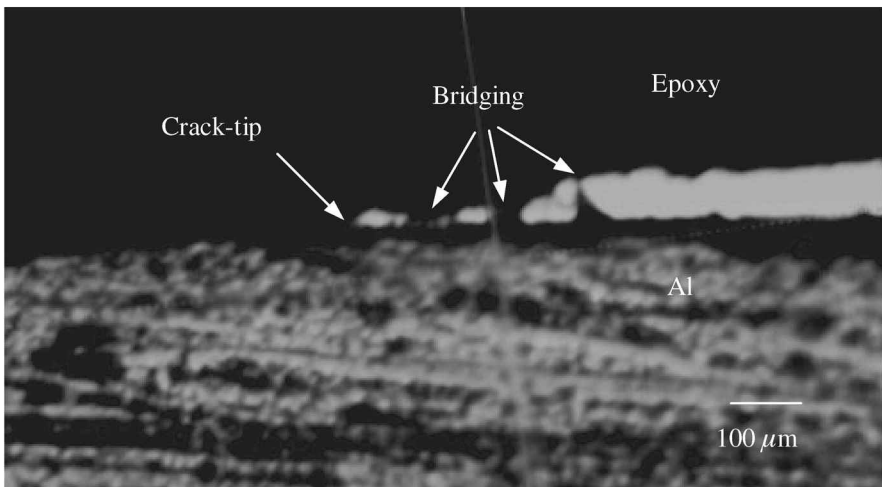

Figure 9. Micrograph showing bridging and surface fluctuations behind an extending interfacial crack (G60).

using an optical microscope on the side surface, this arc-shaped crack front leads to an underestimation of about 0.4 mm to 0.65 mm in the effective crack length. In compiling data in the present experiments, 0.5 mm is thus added to the measured effective crack length. The difference of 0.1 mm in the effective crack length leads to an insignificant difference in the evaluation of fracture energy (less than 1%).

Based on the corrected effective crack length, the interfacial fracture resistance is estimated by the 'beam on an elastic foundation' model. Figure 11 shows
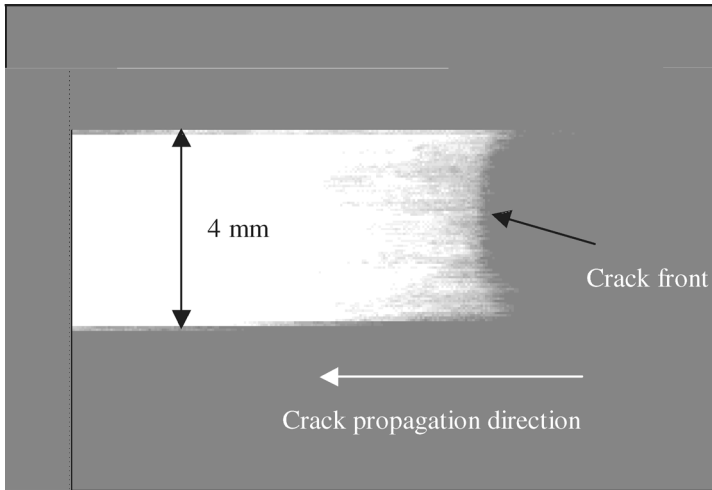
Figure 10. Optical micrograph showing crack front profile.
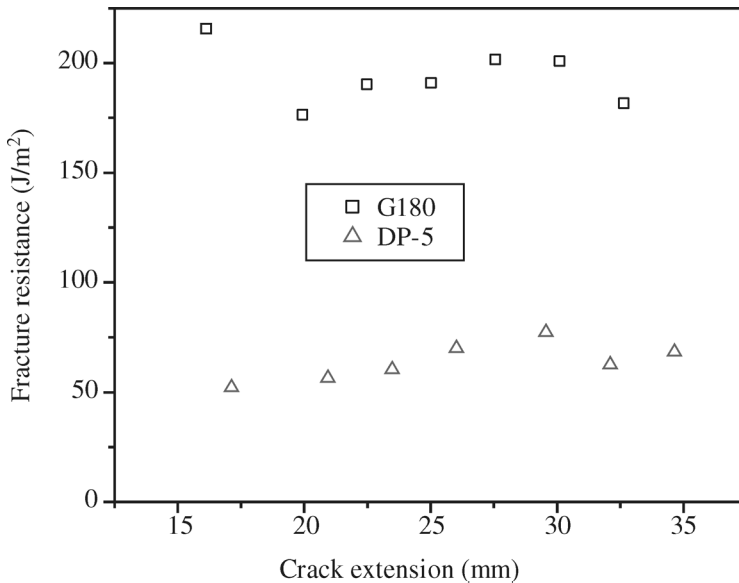
Figure 11. Fracture resistance as a function of the crack extension.

the variation of the fracture resistance in terms of the total debonding length for representative specimens (G180 and DP-5). It is evident that the energy release rate is essentially independent of crack extension. This is generally true for all the other specimens with different surface pretreatments.

Figure 12 shows the dependence of the interfacial fracture resistance on the surface roughness. Each data point along with the error bar in this figure represents the measurements on three specimens that had the same surface treatment. Among all the specimens, the specimen with sapphire substrate has the lowest interfacial fracture resistance, which serves as a baseline of fracture energy for the other specimens. The fracture resistance of specimens with different oxidized surfaces exhibits little variation and is comparable with specimen DP-5, the one with 1 μm diamond paste polished surface. The scatter in the measurements increases with increasing surface roughness. Figure 12 reveals a clear trend that the interfacial fracture resistance is enhanced as surface roughness increases. Note, however, that this relationship is highly non-linear.

6. DISCUSSION

The experimental technique developed in the present study has several advantages. The wedge-peel test using the LDCB specimen provides controlled, stable interfacial crack propagation. From the plot of energy release rate as a function of the crack length for this specimen (Fig. 8), it is evident that the crack propagation is
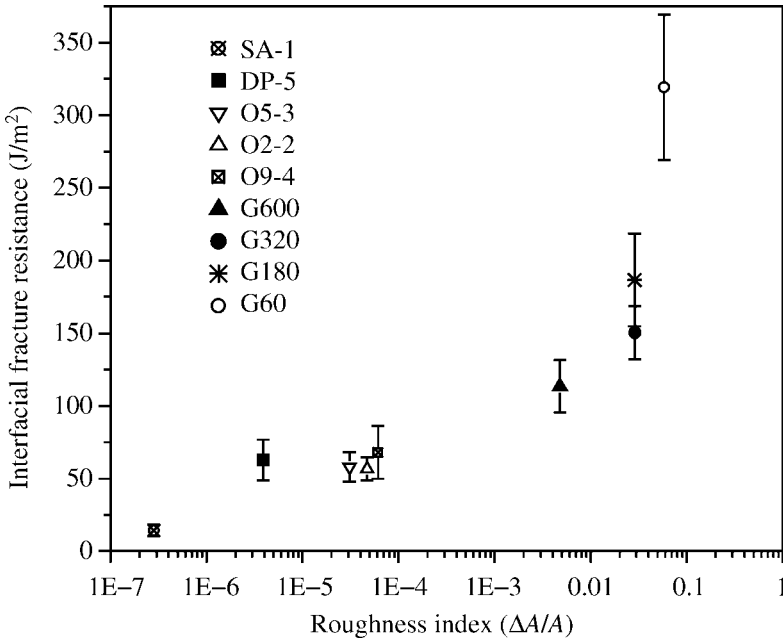

Figure 12. Interfacial fracture resistance as a function of the aluminum surface roughness index.

very stable. Use of the off-white epoxy allows us to monitor the crack front using a video camera; such monitoring would not be possible for three-layered sandwich specimens. Furthermore, the uniform thickness of the wedge simplifies the energy release rate calculation of the specimen. The present authors also tried to use DCDC specimens to measure the interfacial fracture resistance. However, we found that, for this material system, the crack growth in DCDC specimen was rather unstable even with attempts to introduce sharp initial crack by cyclic fatigue.

It should be noted that the interfacial fracture resistance measured in the present experiment is approximately in the same range as that measured by Zhang and Spinks [15], and is somewhat higher than those measured by others [8, 16, 39]. The surface roughness may account for these higher values [15]. The surface roughness gives rise to larger contact surface area between the epoxy and the aluminum substrate, thus requiring higher fracture energy during the peeling process. However, the increase in contact surface area alone would give rise to a linear dependence of the fracture energy on roughness index [37], and cannot explain the present results. The nonlinear dependence of interfacial fracture resistance on surface roughness (see Fig. 12) indicates that other mechanisms [22] must be operative during the fracture process.

Under an optical microscope, bridging was observed behind the extending interfacial cracks for specimens in both groups. Figure 9 shows the bridging in a G60 specimen over a distance of about 250 μm from the crack-tip. The bridging ligaments behind the crack-tip would enhance fracture resistance significantly. A model incorporating a bridging law [40] can be used to evaluate the bridging effect. The waviness of the aluminum surface also suggests the existence of local mixed mode loading at the crack tip, even under far-field Mode-I loading. This will also enhance the interfacial fracture resistance.

To gain an insight into the role of the aluminum surface features in determining the interfacial fracture resistance, we examined the interfaces of the specimens used in the present study. Figure 13 shows SEM images of the epoxy–aluminum interface for a 1 μm diamond paste polished aluminum surface (DP-5) at different magnifications. It can be seen that the interface is perfectly intact when examined with the highest resolution, indicating good epoxy penetration. Figure 14 shows SEM micrographs of epoxy–aluminum interface for an O9-4 specimen. The interface structure in these specimens is quite similar to that for DP-5 in Fig. 13. However, unlike in DP-5 specimens, occasional debonded regions were observed at the epoxy–aluminum interface (Fig. 14b). The rest of the interface, however, was intact as shown in Fig. 14c. The epoxy–aluminum interface for a G60 specimen is shown in Fig. 15. The G60 surface undulations span a length of the order of hundred micrometers, comparable to that of the bridging seen in Fig. 9. The cross-sectional view in Fig. 15 shows large debonded regions (interfacial cracks) at the interface. In Fig. 15b and 15c high-magnification SEM images of the debonded and intact portions, respectively, of the interface of G60 are shown. However, we found that these debonded portions grew in ambient air, indicating that these cracks
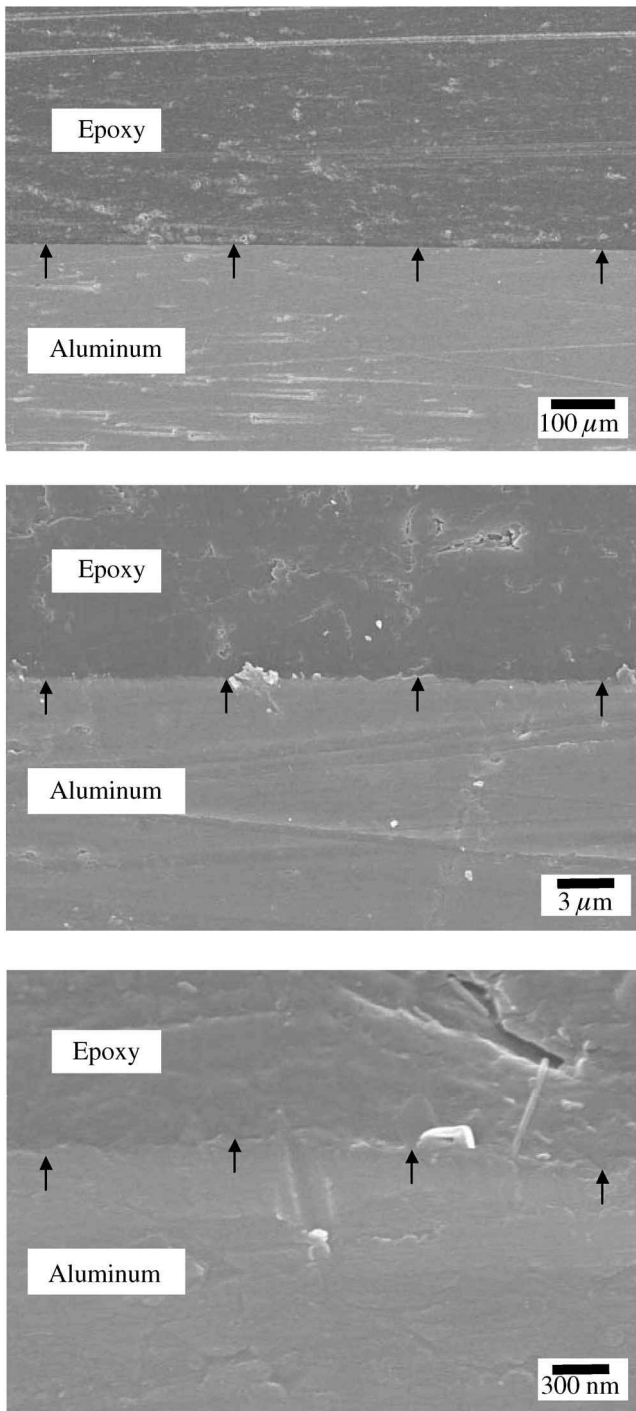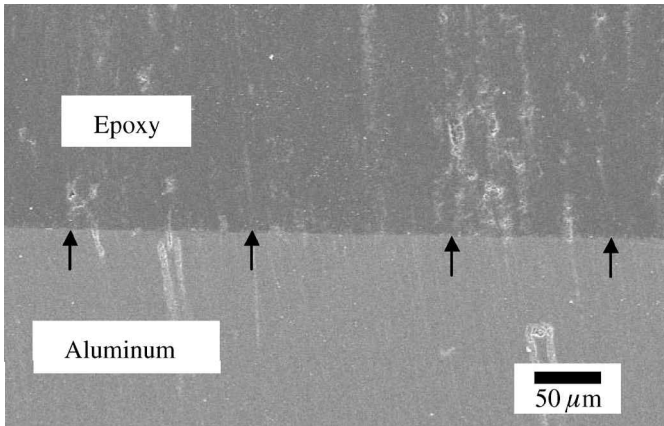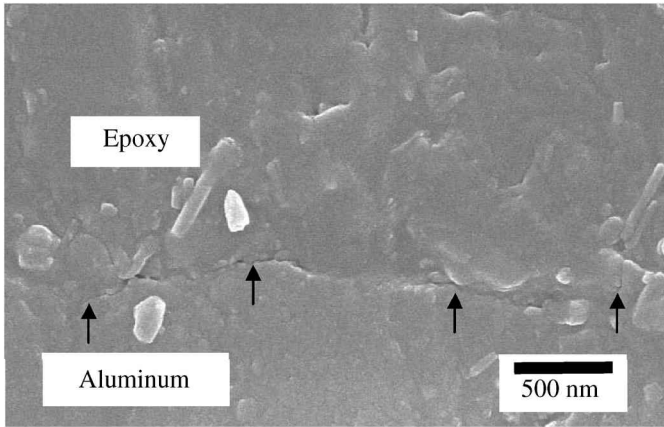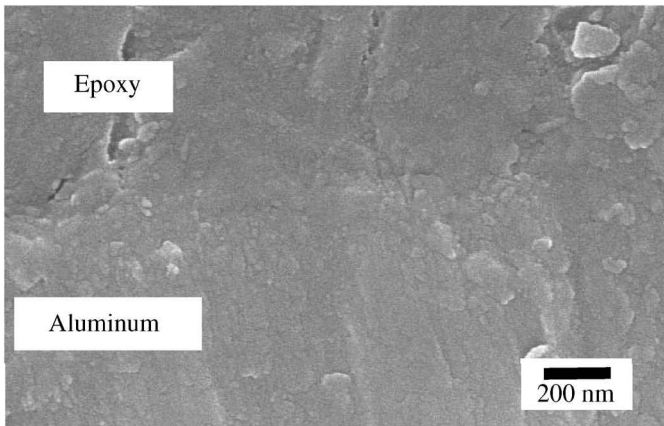
Figure 13. Scanning electron micrographs showing epoxy–aluminum interface for DP-5 at different magnifications. Arrows indicate the location of the interface.
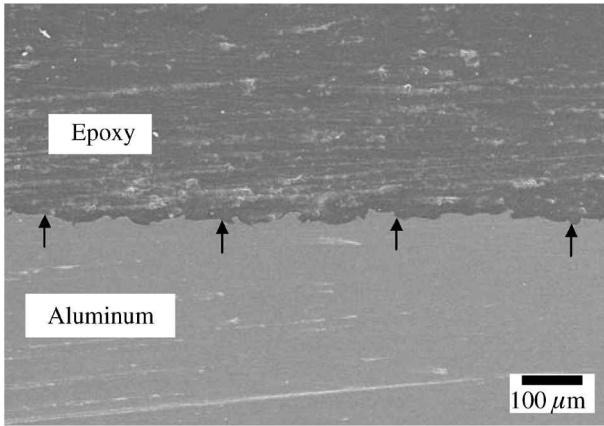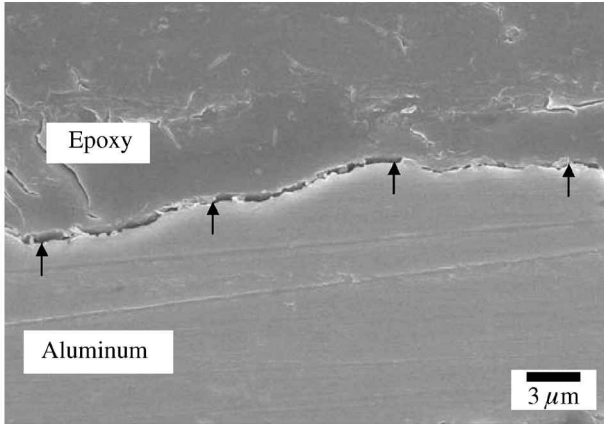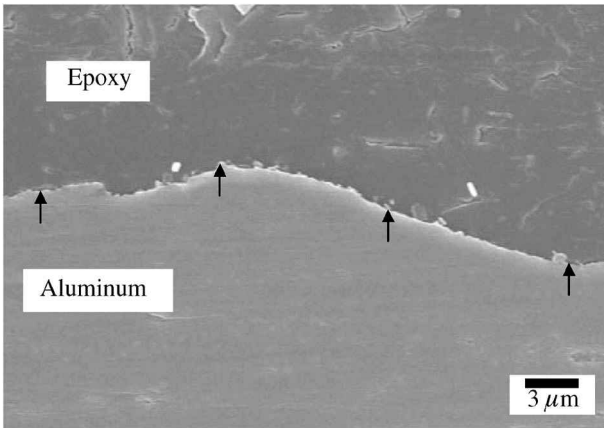
Figure 14. Scanning electron micrograph showing epoxy–aluminum interface for O9-4. (a) Low magnification view; (b) intermittent pores at the interface; (c) intact interface. Arrows indicate the location of the interface.

(a)

(b)

(c)

Figure 15. Scanning electron micrographs showing epoxy–aluminum interface for G60. (a) Roughness highlighting a length scale of tens of micrometers; (b) close-up of separated interface; (c) close-up of intact interface. Arrows indicate the location of the interface.

(Fig. 15b) were likely to have formed during polishing of the cross section rather than during curing of epoxy, and grew under the influence of local residual stress and the environmental moisture [41, 42]. The above observations suggest that crack-tip bridging and mode-mixity play an important role in enhancing the interfacial fracture toughness.

Figure 12 along with Figs 13–15 suggest that, while seeking to identify the relationship between surface morphology and interfacial fracture resistance, features on the appropriate length scale should be considered. For the surfaces considered in the present study, the values of surface roughness index, R, used to characterize the aluminum surfaces may be dependent on the details of measurements. The reason for this is that the surface features may well be fractal in nature [43]. Figure 16 shows three AFM scans of the CRATER treated surface of specimen O9-4 with different resolutions. Figure 16a, b, and c are scans of the same spot on the specimen with full scanned lengths of 140 μm, 14 μm and 350 nm, respectively, corresponding to lateral resolutions of about 400 nm, 40 nm and 1 nm, respectively. It is evident that the roughness features of the surface are self-similar at length scales spanning more than two orders of magnitude, characteristic of a fractal geometry. As a result, the roughness index evaluated by equation (1) has a higher value when using measurements with a higher resolution. In the current study, we used the measurements from profilometer scans to correlate the fracture resistance data in Fig. 12. These measurements have a lateral resolution of about 250 nm, and highlight the roughness features in microscale rather than in nanoscale. As shown in Fig. 9, the dominant processes controlling interfacial fracture, i.e. the bridging and the coalescence of microcracks with the main crack, occur at a length scale of tens of micrometers. Therefore, we believe that the resolution of the profilometer measurements was able to characterize the aluminum surface features (Figs 2–4) in the current work. An indirect evidence of this belief, shown in Table 1 and in Fig. 12, is that the three CRATER-treated surfaces have nearly the same values of roughness index when measured by a profilometer, although their nanoscale features such as the nanoscopic pore sizes are rather different. The interfacial fracture resistance values of these three surfaces are, not surprisingly, essentially equal.

It should be noted that moisture can affect the interfacial fracture characteristics [13, 14] and enhance subcritical crack growth [41, 42] for epoxy–substrate interfaces. Since the primary aim of the present study was to assess the influence of surface morphology on interfacial fracture, no attempt was made to condition the experiments with moisture. We plan to address this issue through experiments in controlled moist environments. The influence of moisture on the variation of interfacial fracture energy with the surface morphology of epoxy–aluminum interfaces would be the subject of future study.

Finally, we note that the roughness index defined in equation (1), R, although an accurate measurement of surface area increase, may not be able to capture the complex features such as mode-mixity and asperity shapes of the interface, let alone the
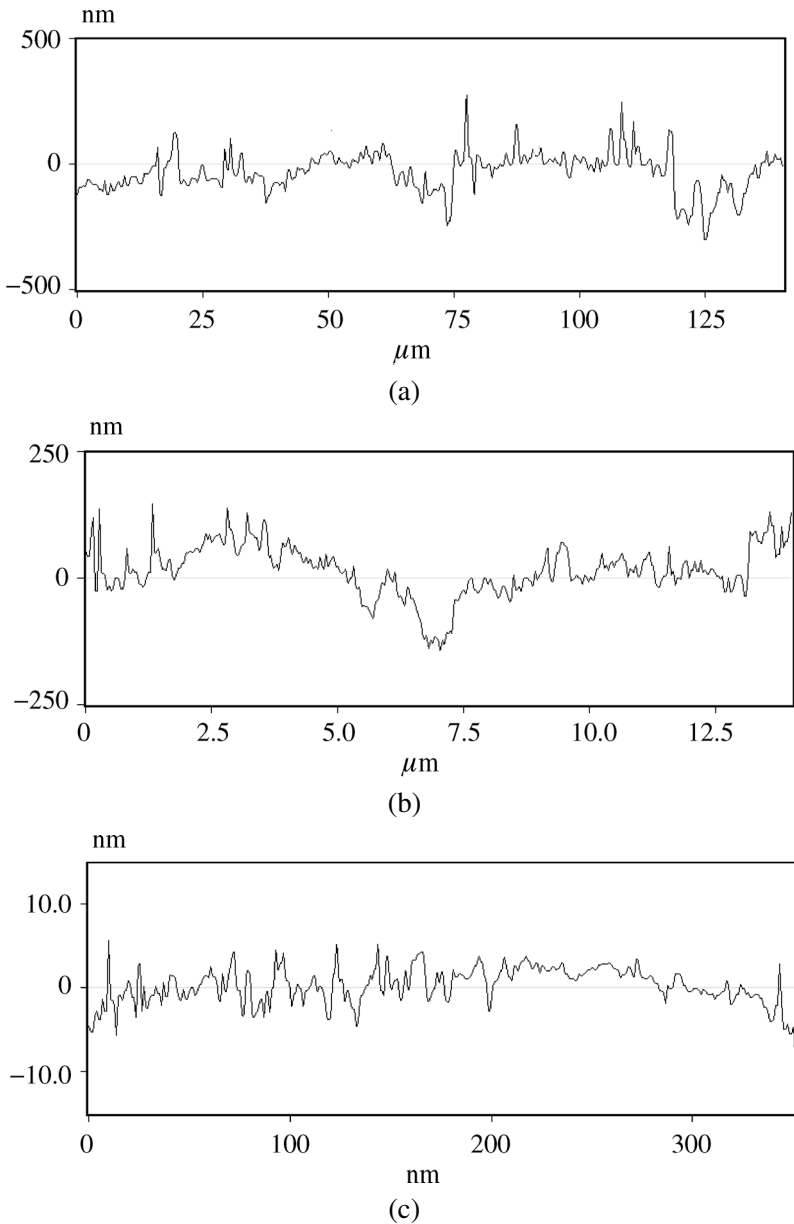
Figure 16. Topologies of specimen O9-4 using AFM scans at a lateral data resolution of (a) 400 nm, (b) 40 nm and (c) 1 nm.

degree of interfacial wetting, local stress state, etc. Further experimental and corresponding theoretical research is needed to isolate and quantify the effect of each possible mechanism affecting interfacial fracture toughness of epoxy–aluminum interfaces.

7. CONCLUSIONS

In the present work, the effects of substrate surface morphology on the fracture resistance of epoxy–aluminum interface are systematically studied. A bi-layer LDCB specimen was chosen to measure the interfacial fracture resistance. This specimen was calibrated by a model consisting of a beam on an elastic foundation which was validated by a finite-element analysis. The experimental results show that increasing surface roughness enhances the interfacial fracture resistance. Non-linearity in this relation indicates that such an enhancement is caused not only by the increase in the actual contact area between the epoxy and the aluminum substrate due to roughness, but also by the change of local mode-mixity, as well as bridging and friction behind the crack. The study shows that the important parameter governing the fracture resistance of epoxy–aluminum interface is the microscopic roughness index rather than the nanoscale surface features of the aluminum surface.

REFERENCES

1. H. M. Clearfield, D. K. McNamara and G. D. Davis, in: *Adhesives and Sealants, ASM Engineered Materials Handbook*, H. F. Brinson (Technical Chairman), Vol. 3, pp. 259–275. ASM International, Metals Park, OH (1990).
2. M. R. Turner, B. J. Dalgleish, M. Y. He and A. G. Evans, *Acta Metall. Mater.* **43**, 3459–3465 (1995).
3. M. R. Turner and A. G. Evans, *Acta Mater.* **44**, 863–871 (1996).
4. A. Cazzato and K. T. Faber, *J. Am. Ceram. Soc.* **80**, 181–188 (1997).
5. M. D. Thouless, *Acta Metall. Mater.* **40**, 1281–1286 (1992).
6. M. D. Thouless, *Scripta Metall. Mater.* **26**, 494–951 (1992).
7. M. Y. He, A. G. Evans and J. W. Hutchinson, *Acta Mater.* **44**, 2963–2971 (1996).
8. M. D. Thouless, M. S. Kafkalidis, S. M. Ward and Y. Bankowski, *Scripta Metall.* **37**, 1081–1087 (1997).
9. A. J. Price and J. P. Sargent, *Int. J. Adhesion Adhesives* **17**, 27–32 (1997).
10. H. Chai, *Composites* **15**, 277–290 (1984).
11. H. Chai, *Eng. Fracture Mech.* **24**, 413–431 (1986).
12. H. Chai, *Int. J. Fracture* **32**, 211–213 (1987).
13. D. M. Brewis and G. W. Critchlow, *Int. J. Adhesion Adhesives* **17**, 33–38 (1997).

14. M. Kalnins, A. Sirmacs and L. Malers, *Int. J. Adhesion Adhesives* **17**, 365–372 (1997).
15. Y. L. Zhang and G. M. Spinks, *J. Adhesion Sci. Technol.* **11**, 207–223 (1997).
16. M. D. Thouless, J. L. Adams, M. S. Kafkalidis, S. M. Ward, R. A. Dickie and G. L. Westerbeek, *J. Mater. Sci.* **33**, 187–197 (1998).
17. J. G. Swadener, K. M. Liechti and A. L. de Lozanne, *J. Mech. Phys. Solids* **47**, 223–258 (1999).
18. A. Mannelqvist and M. R. Groth, *Appl. Phys. A* **73**, 347–355 (2001).
19. E. Sancaktar and R. Gomatam, *J. Adhesion Sci. Technol.* **15**, 97–117 (2001).
20. E. Sancaktar, H. Jozavi, J. Baldwin and R. Gomatam, *J. Adhesion* **23**, 233–262 (1987).
21. E. Sancaktar, S. V. Babu, E. Zhang, G. C. D'Couto and H. Lipshitz, *J. Adhesion* **50**, 103–135 (1995).
22. E. Sancaktar, *J. Adhesion Sci. Technol.* **9**, 119–147 (1995).
23. E. Sancaktar and K. Narayan, *J. Adhesion Sci. Technol.* **13**, 237–271 (1999).
24. J. W. Hutchinson and Z. Suo, *Adv. Appl. Mech.* **29**, 64–189 (1992).
25. A. G. Evans, J. W. Hutchinson and Y. Wei, *Acta Mater.* **47**, 4093–4113 (1999).
26. T. Pardoen and J. W. Hutchinson, *J. Mech. Phys. Solids* **48**, 2467–2512 (2000).
27. S. L. Zhang, K. J. Hsia and A. J. Pearlstein, *J. Mech. Phys. Solids* **50**, 549–569 (2002).
28. S. L. Zhang and K. J. Hsia, *ASME Trans. J. Appl. Mech.* **68**, 93–100 (2001).
29. Z. Suo and J. W. Hutchinson, *Mater. Sci. Eng. A* **107**, 135–143 (1989).
30. H. C. Cao and A. G. Evans, *Mech. Mater.* **7**, 295–305 (1989).
31. S. Yoshida, J. Matsuoka and N. Soga, *J. Am. Ceram. Soc.* **82**, 1621–1623 (1999).
32. S. N. Crichton, M. Tomozawa, J. S. Hayden, T. I. Suratwala and J. H. Campbell, *J. Am. Ceram. Soc.* **82**, 3097–3104 (1999).
33. G. Liu and J. K. Shang, *Metall. Mater. Trans.* **A-27A**, 213–219 (1996).
34. Z. H. Zhang and J. K. Shang, *Metall. Mater. Trans.* **A-27A**, 221–226 (1996).
35. H. Gao, A. Scheeline and A. J. Pearlstein, in: *Proceedings of the International Symposium on New Directions in Electroanalytical Chemistry, II*, J. Leddy, M. D. Porter and P. Vanysek (Eds), Vol. 99-5, pp. 116–124. Electrochemcial Society, Pennington, NJ (1999).
36. H. Gao, A. Scheeline and A. J. Pearlstein, *J. Electrochem. Soc.* **149**, B248–B255 (2002).
37. Y.-B. Xin, K. J. Hsia and D. A. Lange, *J. Am. Ceram. Soc.* **78**, 3201–3208 (1995).
38. M. F. Kanninen, *Int. J. Fracture* **9**, 83–92 (1973).
39. X. Dai, M. V. Brillhart and P. S. Ho, *IEEE Trans. Components Packaging Technol.* **23**, 101–116 (2000).
40. N. Dey, D. F. Socie and K. J. Hsia, *Acta Metall. Mater.* **43**, 2163–2175 (1995).
41. J. E. Ritter, J. D. Fox, D. I. Hutco and T. J. Lardner, *J. Mater. Sci.* **33**, 4581–4588 (1998).
42. J. E. Ritter, A. Huseinovic, S. Chakravarti and T. J. Lardner, *J. Am. Ceram. Soc.* **83**, 2109–2111 (2000).
43. B. B. Mandelbrot, *The Fractal Geometry of Nature*. W. H. Freeman, San Francisco, CA (1982).